Silicate Weathering Dynamics in the Kasaï Basin and Implications for Enhanced Rock Weathering Applications in the Tropics

Yi Hou[1], Lissie W. de Groot[2], Travis W. Drake[2], José Nlandu Wabakanghanzi[3], Alfred Ludjwera Bahati[4], Marijn Bauters[5], Chris Seitz[6], Antoine de Clippele[2], Johan Six[2], Kristof Van Oost[7], Jordon D. Hemingway[1]

[1]Geological Institute, Department of Earth and Planetary Sciences, ETH Zurich, Zurich, Switzerland
[2]Institute of Agricultural Sciences, Department of Environmental Systems Science, ETH Zurich, Zurich, Switzerland
[3]Department of Soil Physics and Hydrology, Congo Atomic Energy Commission, Kinshasa, Democratic Republic of Congo
[4]Régie des Voies Fluviales, Kinshasa, Democratic Republic of Congo
[5]Q-ForestLab, Department of Environment, Ghent University, Ghent, Belgium
[6]Institute of Geochemistry and Petrology, Department of Earth and Planetary Sciences, ETH Zurich, Zurich, Switzerland
[7]Earth and Life Institute, Université catholique de Louvain, Louvain-la-Neuve, Belgium

Key Points:

- Organic acids contribute substantially to the alkalinity budget in the Kasaï Basin.
- Dry deposition and canopy exchange are important solute sources in Kasaï rivers.
- Quantifying carbon sequestered through enhanced rock weathering applications can be particularly complicated in tropical Africa.

Corresponding author: Yi Hou, yihouy@ethz.ch

Abstract

Silicate weathering is one of the ultimate geologic sinks of atmospheric CO_2. Enhanced rock weathering (ERW), aiming at accelerating this natural process to mitigate anthropogenic warming, has received significant attention due to high projected CO_2 removal potential and possible agricultural co-benefits applications in the tropics. Yet, the natural baseline of chemical weathering in low-relief, tropical landscapes, especially central Africa, remains poorly characterized. Here, we systematically sampled river and suspended sediments in the Kasaï Basin, the largest tributary of the Congo River. We constrained chemical weathering dynamics with river solute data and other hydro-chemical/physical observations. We show that organic acids contribute substantially to the alkalinity budget, and, through a mass-balance model, we demonstrate that dry deposition and canopy exchange processes are important solute sources in Kasaï rivers and can bias silicate weathering flux estimates. These complications point to particular challenges in quantifying carbon sequestered through ERW applications in tropical Africa.

Plain Language Summary

The chemical breakdown (i.e. weathering) of silicate rocks consumes atmospheric CO_2 and plays an important role in the global climate and carbon cycle. Despite growing interests in accelerating this natural process to mitigate anthropogenic warming by amending soils with finely crushed rocks (i.e. enhanced rock weathering, ERW) in central Africa, the baseline behavior of chemical weathering in these tropical landscapes remains poorly constrained. In this work, we conducted systematic sampling of rivers in the Kasaï Basin, the largest tributary of the Congo River, and characterized the chemical weathering dynamics. We found that the alkalinity budget, usually composed of inorganic carbon species (products of weathering), can be primarily composed of organic acids in the Kasaï Basin. In addition, forest canopy processes source a substantial amount of river solutes in the Kasaï Basin, which may result in an overestimation of chemical weathering flux. We further discussed these findings in the context of ERW applications in tropical Africa, particularly with respect to site-specific quantification and monitoring of CO_2 sequestration.

1 Introduction

The chemical weathering of silicate minerals, coupled to the burial of calcium carbonate in marine sediments, is one of the ultimate geologic sinks of atmospheric carbon dioxide (CO_2). The temperature dependence of primary mineral dissolution allows for a negative feedback between atmospheric CO_2 levels and silicate weathering flux, and is considered to have, at least partially, regulated planetary climate on geological timescales (Kump et al., 2000; Eiriksdottir et al., 2013). It has been widely acknowledged, however, that other surface processes and environmental conditions (e.g., lithology, erosion rate, and hydrology) can meaningfully impact the rate and intensity of silicate weathering (Bluth & Kump, 1994; Maher & Chamberlain, 2014; West, 2012; Gudbrandsson et al., 2008). How silicate weathering operates under different tectonic and hydroclimatic boundary conditions therefore remains incompletely understood but is crucial in assessing the strength of the climate-weathering feedback and its evolution over time.

On regional to sub-continental scales, rivers integrate weathering signals over their drainage basins by carrying weathering derived solutes and sediments. Understanding weathering processes and quantifying associated fluxes on these spatial scales are thus important for determining global sensitivity from local empirical constraints, as Earth's surface is inherently heterogeneous. However, existing work is heavily biased towards river catchments that either have high weathering rates (e.g., volcanic islands and erosive terrains) or are easily accessible (e.g., northern hemisphere temperate zones). In particu-

lar, the Congo River Basin (Figure 1A), despite being the second largest river by drainage area and discharge, is one of the least studied major river basins on Earth (Alsdorf et al., 2016). Characterized by a wet tropical climate and covered extensively by tropical rain forest, the Congo Basin sits atop some of the longest exposed, most deeply weathered land surfaces on Earth (Braun et al., 2026; Vasconcelos et al., 2019) and is particularly under sampled – filling the observation gaps in these unexplored landscapes is important to better understand chemical weathering in highly productive, low-relief tropical systems. Furthermore, growing interests in enhanced rock weathering applications in the tropics, particularly in central Africa (Schiedung et al., 2026; Haque et al., 2025), warrant first-order characterization of weathering processes in these environments to establish natural baselines.

Enhanced rock weathering (ERW), as a novel CO_2 removal (CDR) strategy to mitigate anthropogenic climate change, aims at speeding up the geological process of silicate weathering by amending soils with finely crushed silicate rocks. Similar to weathering of silicate minerals in natural environments, CO_2 dissolved in surface waters as carbonic acid is converted to bicarbonate and carbonate ions (i.e., carbonate alkalinity) within drainage systems and considered to be durably removed from the atmosphere over millennial timescales. ERW applications in the tropics have recently received significant attention due to high projected CDR potential (Goll et al., 2021) and possible agricultural co-benefits (Swoboda et al., 2022). In particular, hot and humid tropical climate is expected to accelerate mineral dissolution kinetics and hence increase weathering intensity and subsequent alkalinity export. Nutrient addition from rock powder may additionally promote primary productivity and subsequent organic matter storage in soils, potentially contributing to additional CDR (Goll et al., 2021; Edwards et al., 2017). Furthermore, initial pot experiments and field trials with silicate amendments demonstrates promising results of improving soil fertility and increasing crop yield (Swoboda et al., 2025; Conceição et al., 2022; Haque et al., 2019). Given the nutrient depletion of tropical soils and the high food production demand driven by rapid population growth (Meybeck et al., 2017), ERW applications may help meet the challenge of ensuring food security in the Global South, especially in central Africa, despite uncertainties in scalability, durability, and efficiency associated with ERW as a CDR strategy (Schiedung et al., 2026).

In this work, we present new river solute and suspended sediment observations from the Kasaï River Basin, the largest tributary of the Congo River, which features nutrient-poor soils and gradients of hydroclimate and vegetation cover. We constrain the alkalinity budget for the Kasaï rivers and find substantial contribution from organic acids. Contrary to previously reported results for the Congo main stem (Wang et al., 2013), the amount of organic alkalinity does not correlate with the content of dissolved organic carbon due to the presence of highly diverse organic acids across the basin. Using a mass balance model, we additionally demonstrate that up to 60% of river solutes can be sourced from dry deposition and forest canopy processes, potentially biasing silicate weathering flux estimates. We further discuss the implications of these findings for ERW applications in tropical Africa, particularly with respect to site-specific quantification and monitoring of CO_2 sequestration.

2 Materials and Methods

2.1 Study Sites

The Kasaï River Basin (890,000 km^2), is the largest tributary of the Congo River (Fig. 1A). It contributes approximately one-fourth of the Congo River's discharge (Mushi et al., 2019) and exhibits the highest sediment flux ($\sim$10 Tg yr^{-1}) of any tributary in the Congo Basin (Carlier et al., 2026; Laraque et al., 2009; Datok et al., 2021). The Upper Kasaï originates in the Angolan highlands at an altitude of $\sim$1310 m (Van Pul, 2023) and experiences an elevation drop of almost 1000 m before reaching the city of Ilebo (4°19'

S, 20°36' E). In contrast, the lower Kasaï – i.e., from Ilebo to its confluence with the Congo River at Kwamouth (3°10' S, 16°12' E) – exhibits a mere 66 m elevation decrease over the course of ∼600 km (Van Pul, 2023). The Upper Kasaï primarily drains the Angolan Shield (Congo Craton), with minor contributions from Proterozoic metamorphosed sediment and carbonate lithologies (Schlüter, 2006; Jelsma et al., 2018), whereas the Lower Kasaï is underlain by Phanerozoic continental clastic sediments (Schlüter, 2006; Lepersonne, 1974).

Mean annual precipitation (MAP) in the Kasaï Basin is approximately 1500 mm yr^{-1} (Fick & Hijmans, 2017). Unlike the Congo Basin, which straddles the equator, the entire Kasaï Basin lies in the southern hemisphere, where rainfall and discharge are characterized by a single seasonal peak in austral summer. Within the Kasaï Basin, MAP varies between 1000 and 2200 mm yr^{-1} averaging over 1970 and 2000, with MAP decreasing and seasonal variability increasing from north to south (Fick & Hijmans, 2017). Vegetation cover broadly mirrors precipitation patterns, with tropical forests mainly distributed in the north of the basin and predominantly shrubland and savanna in the south (Zanaga et al., 2022). However, rapid population growth in the Kasaï Basin in recent decades (CIESIN, 2018) has resulted in continued deforestation and agricultural conversion (Zhang et al., 2024; Lou et al., 2025), with a recent study estimating that up to one quarter of the basin was cultivated at least once between 2017 and 2024 (Zhao et al., 2026).

2.2 Sample collection, field observations, and analytical methods

A total of 80 samples from 43 rivers in the Kasaï Basin and the Congo River were collected during five field campaigns between August 2022 and August 2024, with 36 rivers sampled in both dry and wet seasons (Figure 1B). Sampled river catchments are described by a limited range of MAP but variable forest coverage (Figure 1C). The Congo River was sampled upstream of Kinshasa (4°18' S, 15°27' E) before Pool Malebo (4°17' S, 15°29' E) twice in August 2022 and January 2024. The main-stem Kasaï River was sampled at multiple locations – before its confluence with the Congo River at Kwamouth, near Bandundu (3°19' S, 17°22' E), and near Ilebo. The major Kasaï tributaries – e.g., Sankuru, Kwilu, Kwango, Lwange, and Fimi rivers – as well as smaller rivers, were sampled immediately upstream of their confluence with the main-stem Kasaï River or their confluence with the higher-order tributaries. Details on river-water sampling, suspended sediment sample collection, field observations (e.g., temperature, pH, discharge), and chemical analyses are described in Supporting Information Text S1.

2.3 Estimating non-carbonate alkalinity

Non-carbonate alkalinity (nCAlk), i.e. the sum of acid neutralizing capacity from deprotonated organic acids (organic alkalinity, OrgAlk) and conjugate bases of other weak acids (other alkalinity, e.g., $B(OH)_4^-$, PO_4^{3-}, HPO_4^{2-}, $H_3SiO_4^-$), was calculated as the difference between total alkalinity (TA) and carbonate alkalinity (CAlk; Morel & Hering, 1983; Wang et al., 2013) following

$$\mathrm{TA} = \underbrace{[\mathrm{HCO_3^-}] + 2 \times [\mathrm{CO_3^{2-}}]}_{\text{carbonate alkalinity (CAlk)}} + \underbrace{[\text{OrgAlk}] + [\text{other alkalinity}]}_{\text{non-carbonate alkalinity (nCAlk)}} + [\mathrm{OH^-}] - [\mathrm{H^+}]. \quad (1)$$

Here, TA was determined by major ion charge balance, and CAlk was determined with CO2SYS (Lewis & Wallace, 1998; Van Heuven et al., 2011; Sharp et al., 2020) using the freshwater option (see Supporting Information Text S2 for details). Error estimates were propagated from analytical uncertainties (2σ) of the solute measurements.

2.4 Mass balance modeling of river solutes

The fractional contribution of different biogeochemical processes to river solutes was constrained using an inverse end-member mixing model (MEANDIR, Kemeny & Tor-

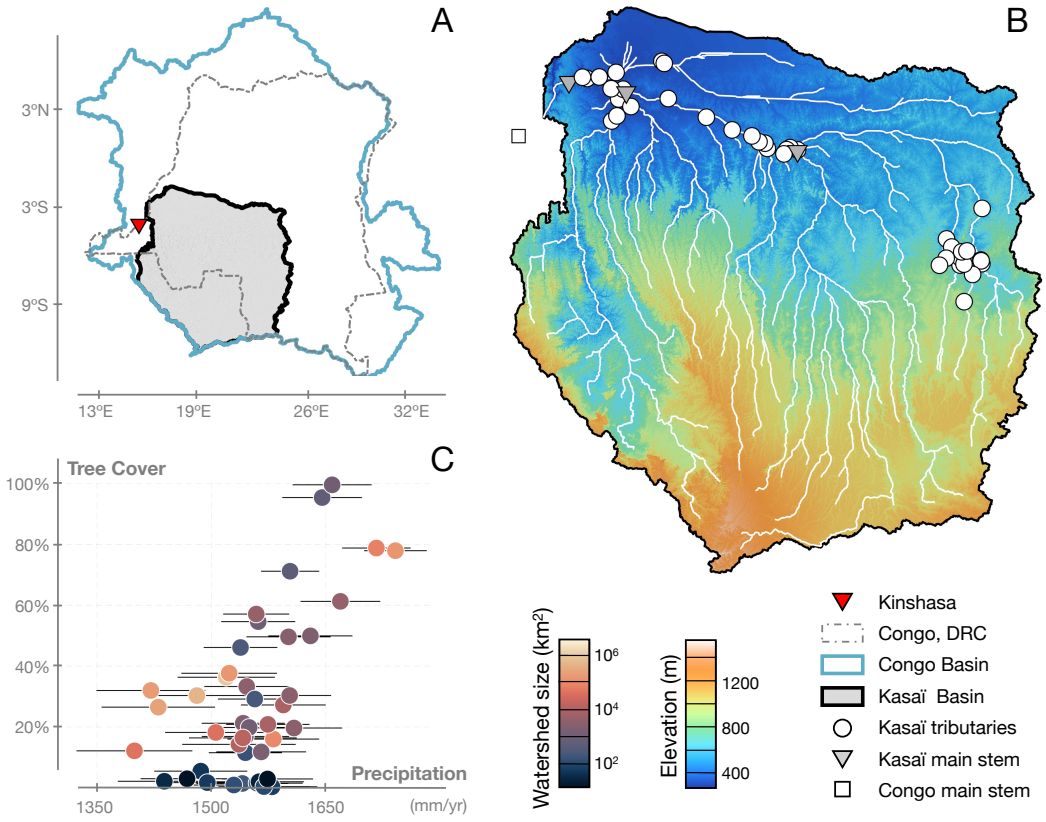

Figure 1. Study site. (A) Map of the Congo Basin (blue outline), the Kasaï Basin (black outline), Democratic Republic of Congo (DRC, gray dashed outline), and the location of Kinshasa (red triangle). (B) Elevation map of the Kasaï Basin projected with WGS 84/UTM Zone 34S. The Digital Elevation Model was acquired using the QGIS SRTM Downloader (Duester, 2024, v3.2.3, NASA server). Samples were collected from the Kasaï tributaries (circles), main-stem Kasaï (triangles), and main-stem Congo (square). (C) catchment percentage of forest cover (Zhao et al., 2026) vs. catchment-averaged MAP (1-km resolution; Fick & Hijmans, 2017), color-coded by watershed size. Error bars represent MAP coefficient of variation.

res, 2021). That is, the normalized concentration of a solute in a given river water sample should equal the sum of the normalized concentration of this solute in all end-members weighed by their fractional contribution (Négrel et al., 1993; Gaillardet et al., 1999; Moon et al., 2014; Burke et al., 2018; Kemeny & Torres, 2021). We specifically let

$$\left(\frac{X_i}{\Sigma^{\pm}}\right)_{\text{riv}} = \sum_{j=1}^{n} f_j \cdot \left(\frac{X_i}{\Sigma^{\pm}}\right)_j, \tag{2}$$

where X_i is the concentration of solute i (= Na^+, Mg^{2+}, Ca^{2+}, K^+, Cl^-, or SO_4^{2-}), $\Sigma^{\pm}$ is the sum of major cation plus sulfate concentration such that

$$\Sigma^{\pm} = [Ca^{2+}] + [Mg^{2+}] + [Na^+] + [K^+] + [SO_4^{2-}], \tag{3}$$

f_j is the fractional contribution of end member j to the total concentration in measured river sample "riv", and n is the number of end members. We opted to include sulfate in the normalization (Eq. 3) to better parameterize the dissolution of sulfide minerals.

Here, we included five end members as major river solute sources in the model – the dissolution of silicate, carbonate, and sulfide minerals; precipitation; and forest canopy throughfall. Importantly, it has been shown that canopy exchange and dry deposition can significantly modify the composition of precipitation and account for substantial ion mass fluxes in forested catchments (Bauters et al., 2021, 2022; Hofhansl et al., 2011). We therefore explicitly included throughfall – the chemistry of which theoretically integrates both canopy processes and aerosol deposition – in the model to account for these processes and more accurately partition river solutes. The composition of the throughfall end member was obtained using a 2-year field measurement time-series from the Yoko Forest Reserve (0°17'N, 25°18'E) in the Congo Basin (Makelele et al., 2022; Bauters et al., 2022).

By solving Eq. 2 using a Monte Carlo inverse approach, our model allows the sometimes large uncertainties in end-member compositions to be treated probabilistically and accounts for potential end-member heterogeneity between different tributaries. For example, the silicate end member at our study sites is not directly constrained, as it is difficult to access and sample fresh, unweathered bedrock in such extensively weathered watersheds overlain by thick regolith. Furthermore, even in the scenario where bulk rock chemistry is available, differences in primary mineral dissolution rates, grain-scale heterogeneity, or uptake by secondary phases may result in nonstoichiometric solute release (Bickle et al., 2015; Ruiz-Agudo et al., 2012; Misra & Froelich, 2012). Similar logic applies to other end members (see Supporting Information Text S3 for a detailed description of all end-member composition parameterizations and model implementation).

3 Results and discussion

3.1 DOC control on the presence of non-carbonate alkalinity

TA exceeds CAlk in 49 out of 80 water samples. Given that conjugate bases of other inorganic weak acids are usually present in negligible amounts in natural freshwater systems, nCAlk should be comprised predominantly of OrgAlk (Eq. 1). We therefore assume OrgAlk ≈ nCAlk in the following discussions. We found the presence of up to ∼200 μEq L^{-1} OrgAlk (one outlier removed; Figure 2A); specifically, OrgAlk dominates over CAlk at low pH (<6) and at low cation load (<200 μEq L^{-1}; Figure 2B). Nevertheless, OrgAlk does not correlate with DOC concentration (Spearman's $\rho = 0.15$, $p = 0.29$; Figure 2A), likely pointing to a diversity of site density (i.e., the number of acidic functional groups per unit of C) and charge density (i.e., the number of *dissociated* acidic functional groups per unit of C) of DOC in the Kasaï Basin.

The charge density of DOC can be estimated by dividing OrgAlk by DOC concentration. The average of calculated DOC charge density for all rivers that have non-zero

OrgAlk is 11.1 μEq (mg C)$^{-1}$ (median = 9.5 μEq (mg C)$^{-1}$; inter-quartile range = 3.7–16.6 μEq (mg C)$^{-1}$; Figure 2C). As natural DOC is composed of complex organic acid mixtures with different dissociation constants (pKa values; Perdue et al., 1984), charge density is a function of pH and approaches site density (i.e., 100% deprotonation) at the high end of natural surface water pH (Hruška et al., 2003). The molecular composition of DOC in our samples is unavailable. Instead, we estimate site density following a triprotic model of organic acid dissociation presented in Hruška et al. (2003) with three apparent pKa values (pK_{a1} = 3.04, pK_{a2} = 4.51, pK_{a3} = 6.46), assuming the same relationship between pH and degree of dissociation. Using this model, we calculate an average DOC site density of 15.4 μEq (mg C)$^{-1}$ (median = 15.2 μEq (mg C)$^{-1}$; inter-quartile range = 5.5–22.8 μEq (mg C)$^{-1}$; Figure 2D). Our average DOC site density estimate for the Kasaï Basin is higher than previously reported values in temperate rivers, which range between 4.6 and 10.2 μeq (mg C)$^{-1}$ (Oliver et al., 1983; Driscoll et al., 1994; Köhler et al., 1999; Hruška et al., 2003; Morel & Hering, 1983), but is similar to exchange acidities of 10.5 and 12.3 μeq (mg C)$^{-1}$ for hydrophobic and hydrophilic acids estimated from forest floor leachates (Vance & David, 1991). This result is consistent with the high normalized chromophoric dissolved organic matter absorbance observed in the Congo River, which has been attributed to elevated organic acid concentrations (Spencer et al., 2009, 2012).

Estimated OrgAlk and site density of DOC can vary substantially between wet and dry seasons in some rivers in the Kasaï Basin (Figure 2D and Figure S1A). Wet-season OrgAlk is higher than that in dry seasons for most rivers (Figure S1A), indicating a strong hydrological control on the production, mobilization, and export of organic acids, conforming to previous observations at the event scale (David et al., 1992). However, seasonal changes in DOC site density are less systematic and do not correlate with the percentage of forest cover in the catchment (Figure 2D), pointing to the high compositional diversity of DOC in tropical rivers (Lambert et al., 2016; Spencer et al., 2016).

On the basin scale, we find that pH – rather than DOC concentration – is a better predictor of the fraction of OrgAlk (Figure 2B, Figure S1B), highlighting the coupling between inorganic and organic carbon cycling. At any given DOC concentration, higher pH promotes more complete organic acid dissociation, therefore generating more OrgAlk, with the variability in the intrinsic properties of DOC (i.e., site density) exerting a secondary control. Meanwhile, higher cationic load and higher CAlk at higher pH result in OrgAlk accounting for a smaller fraction of TA. However, despite exhibiting proportionally less OrgAlk, circumneutral rivers can have similar OrgAlk and CAlk concentrations (Figure 2B), with OrgAlk comparable to that in the acidic, DOC rich, forested rivers (Figure 2A). Such rivers – which sometimes exclusively drain rainforests – often feature low pH, high DOC, low suspended sediment content, and are usually referred to as "blackwater" or "black" rivers due to their dark color (Dupré et al., 1996; Berner & Berner, 2012). Still, as there is no quantitative or formal definition for "blackwater" rivers, we refrained from categorizing the rivers sampled here. Rather, samples form a continuum in environmental parameter space (Figure S2), where pH, DOC concentration, and suspended sediment load all co-vary. The presence of this continuum in Kasaï Basin rivers again highlights that a substantial contribution of organic acids to the TA budget is not limited to "blackwater" rivers on which most previous work has focused.

3.2 Throughfall as an important river solute source

Estimated fractional contributions of each end member (f_j) to each river sample ($\Sigma^{\pm}$; Eq. 3) are shown in Figure S2–S3. Briefly, model results show that f_j values for each end member vary substantially between rivers (Figure S3A): while solute input from pyrite weathering and precipitation are minor in most samples (median $f_{\text{pyrite}} = 0.03$; median $f_{\text{precipitation}} = 0.06$), silicate and carbonate weathering can each supply anywhere between 0 to almost 80% of river solutes (Figure S2A-B). Furthermore, throughfall – an

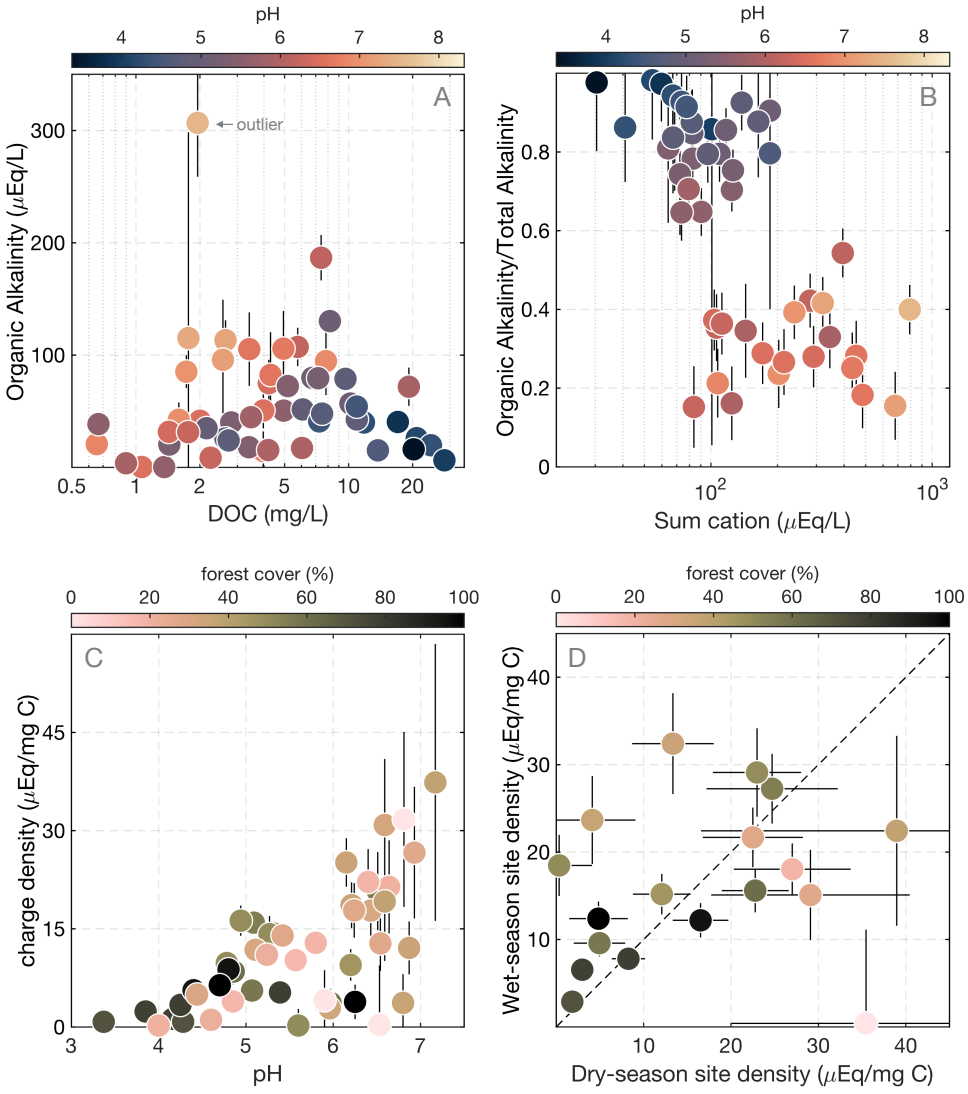

Figure 2. Estimated Alkalinity. Cross plots of (A) organic alkalinity (OrgAlk) concentration vs. DOC concentration (outliers are defined as data points more than three standard deviations from the mean), (B) OrgAlk fraction vs. total cation load, (C) calculated DOC charge density vs. pH, and (D) estimated wet- vs. dry-season DOC site density. Markers are color coded by pH and percentage of forest cover in panels A–B and C–D, respectively. Error bars represent error estimation propagated from analytical uncertainty ($\pm 2\sigma$) of solute measurements.

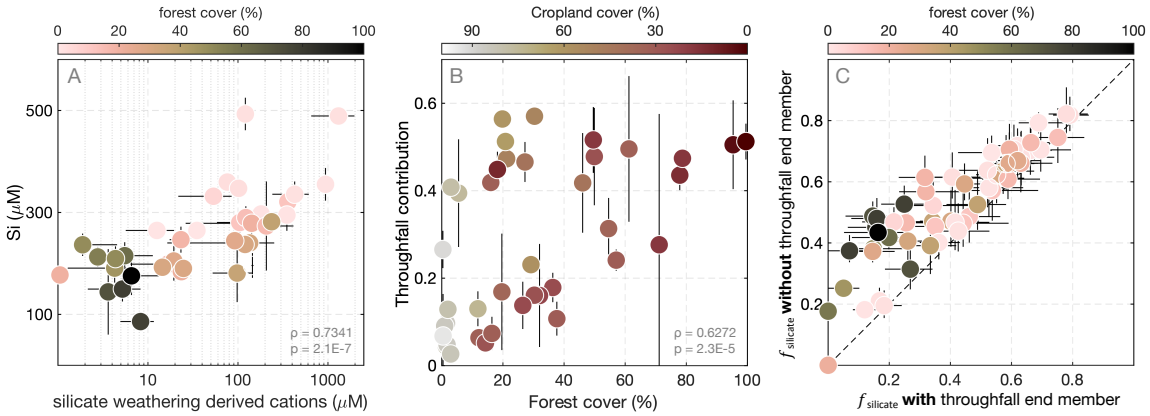

Figure 3. Partitioning of river solutes. Cross plots of: (A) seasonal averages of measured dissolved Si concentration vs. model estimated silicate weathering derived cation concentration, color coded by percentage of catchment forest cover; (B) seasonal averages of model estimated throughfall contribution ($f_{\text{throughfall}}$) vs. percentage of catchment forest cover, color coded by percentage of catchment cropland cover (Zhao et al., 2026); and (C) model estimated silicate weathering contribution without throughfall as an end member vs. with throughfall as an end member, color coded by percentage of catchment forest cover. Error bars represent one standard deviation ($\pm 1\sigma$) in panels A–B and the inter-quartile range of all successful simulations of a given sample (river) in panel C.

end member rarely considered in river chemistry budgets – can contribute up to 60% of river solutes (Figure 3A, S2E). The fractional contributions of different end members also vary by season (Figure S4A-E); however, such seasonal variability is largely site-dependent, as no systematic trend was observed across all rivers (Figure S4F). This is somewhat expected — the substantial variations in the size and other geomorphic attributes between the catchments can lead to considerable variations in their hydrological functioning (Kirchner et al., 2023; Beven et al., 1988).

Our model results are independently validated by measured riverine dissolved Si concentrations (Figure 3A). In the Kasaï Basin, Si cycling is partially decoupled from cation cycling as most river suspended sediments are composed of only quartz (SiO_2) and kaolinite ($Al_2Si_2O_5(OH)_4$; Figure S5), both of which do not contain cations in their crystal structure. We therefore did not include dissolved Si concentration as an additional solute constraint – nor secondary clay formation as an additional end member – in the end-member mixing model. Still, as all dissolved Si in the river is ultimately sourced from the dissolution of primary or secondary silicate minerals, riverine Si concentration should correlate with silicate weathering sourced cation concentrations, calculated as the observed cation concentration times the fractional contribution of silicate weathering estimated by the model (f_{silicate}). Indeed, we observed a positive correlation between Si concentration and independently estimated silicate weathering sourced cation concentrations (Spearman's $\rho = 0.73$, $p = 2.1 \times 10^{-7}$, Figure 3A), which lends confidence to our model results. Several other processes, including uptake by higher plants and the dissolution of biogenic silica (i.e., phytoliths; Alexandre et al., 1997), can modulate Si cycling on the catchment scale, which may partially explain the spread in the data.

Positive correlations were observed between $f_{\text{throughfall}}$, the estimated fractional contribution from throughfall, and (1) the percentage of forest cover in the catchment (Figure 3B; Spearman's $\rho = 0.63$, $p = 2.3 \times 10^{-5}$; Zhao et al., 2026) and (2) the catchment-averaged

aboveground biomass (Figure S6; Spearman's $\rho = 0.63$, $p = 1.1 \times 10^{-5}$; Santoro & Cartus, 2025), highlighting the important role of canopy exchange processes. Interestingly, $f_{\text{throughfall}}$ appears to be more variable in catchments with limited forest cover, possibly reflecting dry deposition. In addition to canopy leaching and uptake, aerosol emissions from prevalent slash-and-burn agricultural practices (Peltier et al., 2014; Tanzito et al., 2020) and high incidence of grassland and savanna fires (Van der Werf et al., 2010) can substantially alter the chemical composition of rainwater. In contrast, no significant correlation was observed between $f_{\text{throughfall}}$ and the extent of either cropland or grassland cover in the catchment, likely due to temporal and spatial stochasticity of natural fires and the evolving nature of croplands in the Kasaï Basin (Zhao et al., 2026). While the quantification of relative solute/mass fluxes from canopy processes vs. dry deposition requires site-specific assumptions (e.g., aerosol composition; Hofhansl et al., 2011) and is beyond the scope of this study, our results nevertheless show that up to ∼60% of river solutes can be sourced from throughfall (which integrates canopy processes *and* dry deposition), particularly in watersheds with extensive forest cover.

Importantly, f_{silicate} may be overestimated if throughfall is not considered in the mass balance. As an experiment, we performed a separate mass balance model without throughfall as an end member. Results show that the estimated silicate weathering contribution is significantly higher for the more forested rivers when throughfall is excluded (Figure 3C). In contrast, the estimated fractional contribution of carbonate weathering remains relatively unchanged (Figure S7A), whereas pyrite weathering and precipitation inputs are marginally overestimated (Figure S7B-C). As the apportionment of river solutes to end-member processes is central in assessing the impact of chemical weathering on the carbon cycle and the climate (e.g., Gaillardet et al., 1999; Bufe et al., 2024), our results suggest that the throughfall input can be an important solute source in tropical rivers that has been previously overlooked. Although the cations in throughfall are ultimately sourced from rock weathering, the aboveground biomass, on the timescale over which it can be considered to be at steady state, is effectively a separate solute source, as the loss of cations to rivers from plant litter does not require "new" silicate weathering to occur (Chadwick et al., 1999; Hedin et al., 2003).

3.3 Silicate weathering within a supply-limited basin and implications for ERW applications

Finally, we evaluate the sensitivity of chemical weathering to erosion in the Kasaï Basin. Cation flux from silicate weathering (in t km^{-2} yr^{-1}; identical to "silicate cation denudation rate" defined in West et al., 2005) was calculated using measured discharge, river solute concentrations, and model-inferred f_{silicate}. Erosion rate (in mm yr^{-1}) was calculated as the sediment flux (i.e., measured surface suspended sediment concentration multiplied by discharge) normalized to drainage area. For watersheds where data are available for both dry and wet seasons, arithmetic means were taken to represent annual averages, as continuous hydrographs over a given year do not exist for these rivers. The estimated cation fluxes of the Congo River and the Kasaï River at Kwamouth are 1.75 and 1.21 t km^{-2} yr^{-1}, respectively, whereas their estimated erosion rates are 0.0034 and 0.0062 mm yr^{-1}. For both the Congo and Kasaï rivers, our estimates are consistent with previously reported mechanical erosion rates (0.0029 and 0.0041 mm yr^{-1}, respectively) and silicate weathering-derived total dissolved solid fluxes after correcting for SiO_2 (1.06 and 1.16 t km^{-2} yr^{-1}, respectively; Figure 4A; Gaillardet et al., 1995). Such consistency implies that basin-scale sediment yield and chemical weathering flux remained relatively unchanged in the Congo and Kasaï rivers over the past 30 years despite considerable anthropogenic perturbation. Nevertheless, we did not explicitly provide any error bounds on our weathering flux and erosion rate estimates as the uncertainties are intrinsically large given the lack of continuous hydrological data.

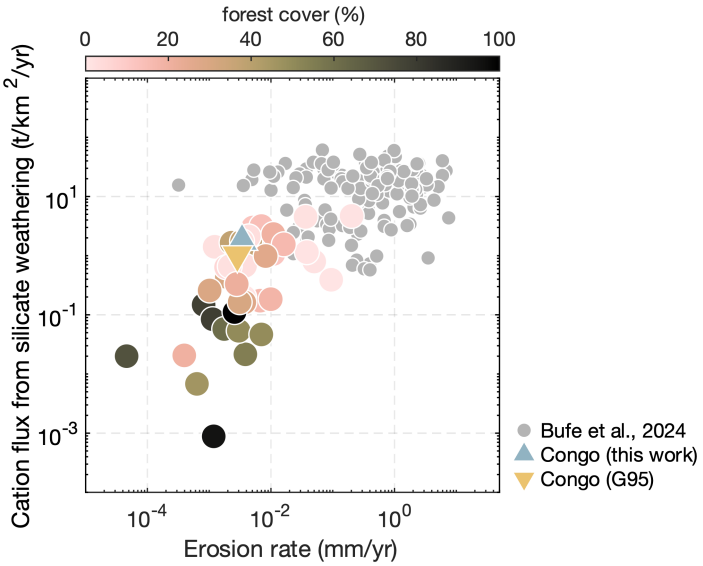

Figure 4. Sensitivity of silicate weathering to erosion. Cross plot of cation flux derived from silicate weathering vs. estimated erosion rate, color coded by percentage of catchment forest cover. Erosive catchments in (Bufe et al., 2024) are denoted in grey circles. The yellow and blue triangles are flux estimates for the Congo River reported in Gaillardet et al. (1995) and in this work, respectively.

Within the Kasaï Basin, four-orders-of-magnitude variability in cation flux from silicate weathering and erosion rates is observed (Figure 4). The more acidic, DOC-rich, forested rivers exhibit some of the lowest cation fluxes from silicate weathering and erosion rates of any river measured to date. Across our entire dataset, cation flux from silicate weathering increases with erosion rate, consistent with previous postulations that CO_2 drawdown from chemical weathering is sensitive to erosion at low erosion rates (i.e., <0.07 mm yr^{-1}, Bufe et al., 2024) and that chemical weathering in the Congo Basin is supply limited (West et al., 2005).

Our comprehensive survey of rivers in the Kasaï Basin carries several implications for ERW applications in tropical Africa. First, given the observed supply limitation and low erosion rates (Figure 4), cation flux is expected to increase with the amendment of rock powder, as long as the hydrologic properties of the soils are not significantly altered. However, it is likely that the increase in cation release does *not* stoichiometrically correspond to contemporaneous atmospheric CO_2 consumption due to high organic acidity (Figure 2). As the neutralization of organic acids by silicate minerals does not directly involve inorganic carbon species, increase in TA is largely driven by increase in OrgAlk rather than CAlk. Although the carbon in OrgAlk is ultimately sourced from atmospheric CO_2, the stability of DOC species that constitute OrgAlk during downstream transport remains largely unknown. More intricately, in the end-member scenario where all mineral dissolution is driven by organic acids instead of carbonic acid, elevated pH will still favor the partitioning of DIC as bicarbonate and carbonate ions, and may counteract CO_2 degassing from organic matter degradation. Therefore, determining whether OrgAlk generated by ERW applications counts as sequestered carbon for monitoring, reporting, and verification (MRV) can be elusive. Furthermore, due to the intermittent nature of small-holder agriculture prevalent in central Africa (Zhao et al., 2026), river catchment-scale monitoring may be more practical than plot scale monitoring beyond the trial phase. As illustrated earlier, however, canopy processes and dry deposition are additional so-

lute sources, calling for site-specific MRV procedures that constrains carbon mass balance and account for baseline behaviors on the watershed scale.

Open Research Section

All data generated as part of this study can be accessed at `here` during the peer review process and will be made public and deposited permanently in `Zenodo` upon publication of this manuscript.

Inclusion in Global Research Statement

We thank the Régie des Voies Fluviales (RVF, DR Congo), the International Institute of Tropical Agriculture (IITA, Ibadan, Nigeria), and the Woodwell Climate Research Center (Woods Hole, Massachusetts, USA) for their partnership, facilitation, and support during all field campaigns. We thank all crew members and staff of the Kauka vessel for their dedication and guidance in navigating waterways of the Kasaï River basin. Fieldwork was conducted under research permits granted to the TropSEDs project scientific research team by the Ministère de l'Environnement et Développement Durable, DR Congo.

Conflict of Interest declaration

The authors declare no conflicts of interest.

Acknowledgments
This study is part of a project that has received funding from the Swiss National Science Foundation (SNSF) under the Sinergia project "Tropical Soil Erosion Dynamics (TropSEDs)" (CRSII5_205998). We thank Jörg Rickli and Corey Archer for help with ICP-MS measurements.

References

Alexandre, A., Meunier, J.-D., Colin, F., & Koud, J.-M. (1997). Plant impact on the biogeochemical cycle of silicon and related weathering processes. *Geochimica et cosmochimica acta*, *61*(3), 677–682.

Alsdorf, D., Beighley, E., Laraque, A., Lee, H., Tshimanga, R., O'Loughlin, F., ... Spencer, R. G. (2016). Opportunities for hydrologic research in the congo basin. *Reviews of Geophysics*, *54*(2), 378–409.

Bauters, M., Drake, T. W., Wagner, S., Baumgartner, S., Makelele, I. A., Bodé, S., ... Boeckx, P. (2021). Fire-derived phosphorus fertilization of african tropical forests. *Nature Communications*, *12*(1), 5129.

Bauters, M., Janssens, I. A., Wasner, D., Doetterl, S., Vermeir, P., Griepentrog, M., ... Boeckx, P. (2022). Increasing calcium scarcity along afrotropical forest succession. *Nature Ecology & Evolution*, *6*(8), 1122–1131.

Berner, E. K., & Berner, R. A. (2012). *Global environment: water, air, and geochemical cycles*. Princeton University Press.

Beven, K. J., Wood, E. F., & Sivapalan, M. (1988). On hydrological heterogeneity—catchment morphology and catchment response. *Journal of hydrology*, *100*(1-3), 353–375.

Bickle, M. J., Tipper, E., Galy, A., Chapman, H., & Harris, N. (2015). On discrimination between carbonate and silicate inputs to himalayan rivers. *American Journal of Science*, *315*(2), 120–166.

Bluth, G. J., & Kump, L. R. (1994). Lithologic and climatologic controls of river chemistry. *Geochimica et Cosmochimica Acta*, *58*(10), 2341–2359.

Braun, J.-J., Kadima Kabongo, E., Audry, S., Delpomdor, F., Delvaux, D., Mambwe, P., ... Thiéblemont, D. (2026). Geology and geodynamics evolution of the congo basin. In *Resilience and sustainability in the congo basin: Retracing the past, looking to the future* (pp. 1–38). Springer.

Bufe, A., Rugenstein, J. K., & Hovius, N. (2024). CO_2 drawdown from weathering is maximized at moderate erosion rates. *Science*, *383*(6687), 1075–1080.

Burke, A., Present, T. M., Paris, G., Rae, E. C., Sandilands, B. H., Gaillardet, J., ... Adkins, J. F. (2018). Sulfur isotopes in rivers: Insights into global weathering budgets, pyrite oxidation, and the modern sulfur cycle. *Earth and Planetary Science Letters*, *496*, 168–177.

Carlier, N., Barthel, M., de Clippele, A., de Groot, L. W., Drake, T. W., Hemingway, J. D., ... Van Oost, K. (2026). A new sediment budget for the congo river basin reveals underestimated tributary contributions and large-scale deposition. *EGUsphere*, *2026*, 1–35. Retrieved from `https://egusphere.copernicus.org/preprints/2026/egusphere-2026-247/` doi: 10.5194/egusphere-2026-247

Chadwick, O. A., Derry, L. A., Vitousek, P. M., Huebert, B. J., & Hedin, L. O. (1999). Changing sources of nutrients during four million years of ecosystem development. *Nature*, *397*(6719), 491–497.

CIESIN. (2018). *Gridded population of the world, version 4 (gpwv4): Basic demographic characteristics, revision 11.* NASA Socioeconomic Data and Applications Center (SEDAC) Palisades, NY, USA.

Conceição, L. T., Silva, G. N., Holsback, H. M. S., de Figueiredo Oliveira, C., Marcante, N. C., de Souza Martins, É., ... Santos, E. F. (2022). Potential of basalt dust to improve soil fertility and crop nutrition. *Journal of Agriculture and Food Research*, *10*, 100443.

Coplen, T. B. (1988). Normalization of oxygen and hydrogen isotope data. *Chemical Geology: Isotope Geoscience Section*, *72*(4), 293–297.

Datok, P., Sauvage, S., Fabre, C., Laraque, A., Ouillon, S., Moukandi N'kaya, G., & Sanchez-Perez, J.-M. (2021). Sediment balance estimation of the 'cuvette centrale'of the congo river basin using the swat hydrological model. *Water*, *13*(10), 1388.

David, M. B., Vance, G. F., & Kahl, J. S. (1992). Chemistry of dissolved organic carbon and organic acids in two streams draining forested watersheds. *Water Resources Research*, *28*(2), 389–396.

De Schrijver, A., Geudens, G., Augusto, L., Staelens, J., Mertens, J., Wuyts, K., ... Verheyen, K. (2007). The effect of forest type on throughfall deposition and seepage flux: a review. *Oecologia*, *153*(3), 663–674.

Drake, T. W., Guillemette, F., Hemingway, J. D., Chanton, J. P., Podgorski, D. C., Zimov, N. S., & Spencer, R. G. (2018). The ephemeral signature of permafrost carbon in an Arctic fluvial network. *Journal of Geophysical Research: Biogeosciences*, *123*, 1475–1485.

Driscoll, C. T., Lehtinen, M. D., & Sullivan, T. J. (1994). Modeling the acid-base chemistry of organic solutes in adirondack, new york, lakes. *Water Resources Research*, *30*(2), 297–306.

Duester, H. (2024). *Srtm-downloader.* QGIS Python Plugins Repository. Retrieved from `https://plugins.qgis.org/plugins/SRTM-Downloader/`

Dupré, B., Gaillardet, J., Rousseau, D., & Allègre, C. J. (1996). Major and trace elements of river-borne material: the congo basin. *Geochimica et Cosmochimica Acta*, *60*(8), 1301–1321.

Edwards, D. P., Lim, F., James, R. H., Pearce, C. R., Scholes, J., Freckleton, R. P., & Beerling, D. J. (2017). Climate change mitigation: potential benefits and pitfalls of enhanced rock weathering in tropical agriculture. *Biology letters*, *13*(4).

Eiriksdottir, E. S., Gislason, S. R., & Oelkers, E. H. (2013). Does temperature or

runoff control the feedback between chemical denudation and climate? Insights from NE Iceland. *Geochimica et Cosmochimica Acta*, *107*, 65–81.

Fick, S. E., & Hijmans, R. J. (2017). Worldclim 2: new 1-km spatial resolution climate surfaces for global land areas. *International journal of climatology*, *37*(12), 4302–4315.

Gaillardet, J., Dupré, B., & Allègre, C. J. (1995). A global geochemical mass budget applied to the Congo Basin rivers: erosion rates and continental crust composition. *Geochimica et Cosmochimica Acta*, *59*(17), 3469–3485.

Gaillardet, J., Dupré, B., Louvat, P., & Allegre, C. (1999). Global silicate weathering and CO_2 consumption rates deduced from the chemistry of large rivers. *Chemical geology*, *159*(1-4), 3–30.

Gehre, M., Geilmann, H., Richter, J., Werner, R., & Brand, W. (2004). Continuous flow $^{2}H/^{1}H$ and $^{18}O/^{16}O$ analysis of water samples with dual inlet precision. *Rapid communications in mass spectrometry*, *18*(22), 2650–2660.

Gladney, E. S., & Roelandts, I. (1988). 1987 compilation of elemental concentration data for USGS BHVO-1, MAG-1, QLO-1, RGM-1, SCo-1, SDC-1, SGR-1 and STM-1. *Geostandards Newsletter*, *12*(2), 253–362.

Goll, D. S., Ciais, P., Amann, T., Buermann, W., Chang, J., Eker, S., ... others (2021). Potential co2 removal from enhanced weathering by ecosystem responses to powdered rock. *Nature Geoscience*, *14*(8), 545–549.

Gran, G. (1952). Determination of the equivalence point in potentiometric titrations. Part II. *Analyst*, *77*(920), 661–671.

Gudbrandsson, S., Wolff-Boenisch, D., Gislason, S., & Oelkers, E. (2008). Dissolution rates of crystalline basalt at pH 4 and 10 and 25–75 °C. *Mineralogical Magazine*, *72*(1), 155–158.

Haque, F., Clementi, V. J., Möller, B., Bastianini, L., Odhiambo, C., Sagina, S., & Davies, S. (2025). The agronomic impact of enhanced weathering deployments in Sub-saharan africa: Insights from a smallholder field trial in kisumu county, kenya. In *Egu general assembly conference abstracts* (pp. EGU25–7491).

Haque, F., Santos, R. M., Dutta, A., Thimmanagari, M., & Chiang, Y. W. (2019). Co-benefits of wollastonite weathering in agriculture: Co2 sequestration and promoted plant growth. *ACS omega*, *4*(1), 1425–1433.

Hedin, L. O., Vitousek, P. M., & Matson, P. A. (2003). Nutrient losses over four million years of tropical forest development. *Ecology*, *84*(9), 2231–2255.

Hofhansl, F., Wanek, W., Drage, S., Huber, W., Weissenhofer, A., & Richter, A. (2011). Topography strongly affects atmospheric deposition and canopy exchange processes in different types of wet lowland rainforest, southwest costa rica. *Biogeochemistry*, *106*(3), 371–396.

Hruška, J., Köhler, S., Laudon, H., & Bishop, K. (2003). Is a universal model of organic acidity possible: Comparison of the acid/base properties of dissolved organic carbon in the boreal and temperate zones. *Environmental science & technology*, *37*(9), 1726–1730.

Jelsma, H. A., McCourt, S., Perritt, S. H., & Armstrong, R. A. (2018). The geology and evolution of the angolan shield, congo craton. In S. Siegesmund, M. A. S. Basei, P. Oyhantçabal, & S. Oriolo (Eds.), *Geology of southwest gondwana* (pp. 217–239). Cham: Springer International Publishing. Retrieved from `https://doi.org/10.1007/978-3-319-68920-3_9`

Kemeny, P. C., & Torres, M. A. (2021). Presentation and applications of mixing elements and dissolved isotopes in rivers (MEANDIR), a customizable MATLAB model for Monte Carlo inversion of dissolved river chemistry. *American Journal of Science*, *321*(5), 579–642.

Kirchner, J. W., Benettin, P., & van Meerveld, I. (2023). Instructive surprises in the hydrological functioning of landscapes. *Annual Review of Earth and Planetary Sciences*, *51*, 277–299.

Köhler, S., Hru ka, J., & Bishop, K. (1999). Influence of organic acid site density on

ph modeling of swedish lakes. *Canadian Journal of Fisheries and Aquatic Sciences*, *56*(8), 1461–1470.

Kump, L. R., Brantley, S. L., & Arthur, M. A. (2000). Chemical weathering, atmospheric CO_2, and climate. *Annual Review of Earth and Planetary Sciences*, *28*(1), 611–667.

Lambert, T., Bouillon, S., Darchambeau, F., Massicotte, P., & Borges, A. V. (2016). Shift in the chemical composition of dissolved organic matter in the congo river network. *Biogeosciences*, *13*(18), 5405–5420.

Laraque, A., Bricquet, J. P., Pandi, A., & Olivry, J. C. (2009). A review of material transport by the congo river and its tributaries. *Hydrological Processes: An International Journal*, *23*(22), 3216–3224.

Lepersonne, J. (1974). *Carte géologique du zaïre, échelle 1: 2.000. 000.* République du Zaïre, Commissariat d'état aux mines, Service géologique.

Lewis, E., & Wallace, D. (1998). *Program developed for CO_2 system calculations* (Tech. Rep.). Environmental System Science Data Infrastructure for a Virtual Ecosystem.

Lou, Z., Peng, D., Shi, Z., Wang, H., Liu, K., Zhang, Y., ... others (2025). An annual cropland extent dataset for africa at 30 m spatial resolution from 2000 to 2022. *Earth System Science Data*, *17*(8), 3777–3796.

Maher, K., & Chamberlain, C. (2014). Hydrologic regulation of chemical weathering and the geologic carbon cycle. *Science*, *343*(6178), 1502–1504.

Makelele, I. A., Bauters, M., Verheyen, K., Barthel, M., Six, J., Rütting, T., ... Boeckx, P. (2022). Conservative N cycling despite high atmospheric deposition in early successional african tropical lowland forests. *Plant and Soil*, *477*(1), 743–758.

Meybeck, A., Laval, E., Lévesque, R., & Parent, G. (2017). Food security and nutrition in the age of climate change. In *Proceedings of the international symposium organized by the government of québec in collaboration with fao. québec city* (p. 132).

Misra, S., & Froelich, P. N. (2012). Lithium isotope history of cenozoic seawater: changes in silicate weathering and reverse weathering. *science*, *335*(6070), 818–823.

Moon, S., Chamberlain, C., & Hilley, G. (2014). New estimates of silicate weathering rates and their uncertainties in global rivers. *Geochimica et Cosmochimica Acta*, *134*, 257–274.

Morel, F., & Hering, J. G. (1983). Principles and applications of aquatic chemistry. *(No Title)*.

Mullin, J., & Riley, J. (1955). The colorimetric determination of silicate with special reference to sea and natural waters. *Analytica Chimica Acta*, *12*, 162–176.

Mushi, C., Ndomba, P., Trigg, M., Tshimanga, R., & Mtalo, F. (2019). Assessment of basin-scale soil erosion within the congo river basin: A review. *Catena*, *178*, 64–76.

Neal, C. O. (2001). Alkalinity measurements within natural waters: towards a standardised approach. *Science of the Total Environment*, *265*(1-3), 99–113.

Négrel, P., Allègre, C. J., Dupré, B., & Lewin, E. (1993). Erosion sources determined by inversion of major and trace element ratios and strontium isotopic ratios in river water: the congo basin case. *Earth and Planetary Science Letters*, *120*(1-2), 59–76.

Oliver, B. G., Thurman, E. M., & Malcolm, R. L. (1983). The contribution of humic substances to the acidity of colored natural waters. *Geochimica et Cosmochimica Acta*, *47*(11), 2031–2035.

Peltier, R., Dubiez, É., Diowo, S., Gigaud, M., Marien, J.-N., Marquant, B., ... Vermeulen, C. (2014). Assisted natural regeneration in slash-and-burn agriculture: Results in the democratic republic of the congo. *Bois et Forêts des Tropiques*, *321*(3).

Perdue, E., Reuter, J., & Parrish, R. (1984). A statistical model of proton binding by humus. *Geochimica et Cosmochimica Acta*, *48*(6), 1257–1263.

Ruiz-Agudo, E., Putnis, C. V., Rodriguez-Navarro, C., & Putnis, A. (2012). Mechanism of leached layer formation during chemical weathering of silicate minerals. *Geology*, *40*(10), 947–950.

Santoro, M., & Cartus, O. (2025). *ESA Biomass Climate Change initiative (Biomass_cci): Global datasets of forest above-ground biomass for the years 2007, 2010, 2015, 2016, 2017, 2018, 2019, 2020, 2021 and 2022, v6.0.* NERC EDS Centre for Environmental Data Analysis. Retrieved from `https://catalogue.ceda.ac.uk/uuid/95913ffb6467447ca72c4e9d8cf30501`

Schiedung, M., Harrington, K. J., Dupla, X., Möller, B., Facq, E., Sweere, T., ... Hemingway, J. D. (2026). Uncertainties of enhanced rock weathering for climate-change mitigation. *Nature reviews earth & environment*, 1–14.

Schlüter, T. (2006). *Geological atlas of africa: with notes on stratigraphy, tectonics, economic geology, geohazards and geosites of each country*. Springer.

Sharp, J., Pierrot, D., Humphreys, M., Epitalon, J., Orr, J., Lewis, E., & Wallace, D. (2020). *CO_2-System-Extd, v3. 0.1, MATLAB (MathWorks).*

Spencer, R. G., Hernes, P. J., Aufdenkampe, A. K., Baker, A., Gulliver, P., Stubbins, A., ... others (2012). An initial investigation into the organic matter biogeochemistry of the congo river. *Geochimica et Cosmochimica Acta*, *84*, 614–627.

Spencer, R. G., Hernes, P. J., Dinga, B., Wabakanghanzi, J. N., Drake, T. W., & Six, J. (2016). Origins, seasonality, and fluxes of organic matter in the congo river. *Global Biogeochemical Cycles*, *30*(7), 1105–1121.

Spencer, R. G., Stubbins, A., Hernes, P. J., Baker, A., Mopper, K., Aufdenkampe, A. K., ... others (2009). Photochemical degradation of dissolved organic matter and dissolved lignin phenols from the congo river. *Journal of Geophysical Research: Biogeosciences*, *114*(G3).

Swoboda, P., de Souza Martins, E., Vilela, G. F., Ferreira, L., Silveira, C. A. P., Marchi, G., ... others (2025). An assessment of the agronomic benefits of silicate rock powders in brazil in the context of a novel classification.

Swoboda, P., Döring, T. F., & Hamer, M. (2022). Remineralizing soils? the agricultural usage of silicate rock powders: A review. *Science of The Total Environment*, *807*, 150976.

Tanzito, G., Ibanda, P., Talaguma, R., & Lusanga, N. (2020). Slash-and-burn agriculture, the major cropping system in the region of faradje in democratic republic of congo: Ecological and socio-economic consequences. *Journal of Development and Agricultural Economics*, *12*(1), 25–36.

Vance, G. F., & David, M. B. (1991). Chemical characteristics and acidity of soluble organic substances from a northern hardwood forest floor, central maine, usa. *Geochimica et Cosmochimica Acta*, *55*(12), 3611–3625.

Van der Werf, G. R., Randerson, J. T., Giglio, L., Collatz, G., Mu, M., Kasibhatla, P. S., ... van Leeuwen, T. T. (2010). Global fire emissions and the contribution of deforestation, savanna, forest, agricultural, and peat fires (1997–2009). *Atmospheric chemistry and physics*, *10*(23), 11707–11735.

Van Heuven, S., Pierrot, D., Rae, J., Lewis, E., & Wallace, D. (2011). MATLAB program developed for CO_2 system calculations. *(No Title)*.

Van Pul, P. (2023). The upper-kasai watershed. In *Hydrography and navigation on the congo river: A century of visual history* (pp. 43–47). Cham: Springer International Publishing. Retrieved from `https://doi.org/10.1007/978-3-031-41065-9_7` doi: 10.1007/978-3-031-41065-9_7

Vasconcelos, P. M., Farley, K. A., Stone, J., Piacentini, T., & Fifield, L. K. (2019). Stranded landscapes in the humid tropics: Earth's oldest land surfaces. *Earth and Planetary Science Letters*, *519*, 152–164.

Wang, Z. A., Bienvenu, D. J., Mann, P. J., Hoering, K. A., Poulsen, J. R., Spencer,

R. G., & Holmes, R. M. (2013). Inorganic carbon speciation and fluxes in the Congo River. *Geophysical Research Letters*, *40*(3), 511–516.

Werner, R. A., & Brand, W. A. (2001). Referencing strategies and techniques in stable isotope ratio analysis. *Rapid Communications in Mass Spectrometry*, *15*(7), 501–519.

West, A. J. (2012). Thickness of the chemical weathering zone and implications for erosional and climatic drivers of weathering and for carbon-cycle feedbacks. *Geology*, *40*(9), 811–814.

West, A. J., Galy, A., & Bickle, M. (2005). Tectonic and climatic controls on silicate weathering. *Earth and Planetary Science Letters*, *235*(1-2), 211–228.

Yeghicheyan, D., Aubert, D., Bouhnik-Le Coz, M., Chmeleff, J., Delpoux, S., Djouraev, I., ... Suchorski, K. (2019). A new interlaboratory characterisation of silicon, rare earth elements and twenty-two other trace element concentrations in the natural river water certified reference material SLRS-6 (NRC-CNRC). *Geostandards and Geoanalytical Research*, *43*(3), 475–496.

Zanaga, D., Van De Kerchove, R., Daems, D., De Keersmaecker, W., Brockmann, C., Kirches, G., ... others (2022). Esa worldcover 10 m 2021 v200.

Zhang, X., Zhao, T., Xu, H., Liu, W., Wang, J., Chen, X., & Liu, L. (2024). Glc_fcs30d: the first global 30 m land-cover dynamics monitoring product with a fine classification system for the period from 1985 to 2022 generated using dense-time-series landsat imagery and the continuous change-detection method. *Earth System Science Data*, *16*(3), 1353–1381.

Zhao, P., Carlier, N., Ou, X., Wanlin, G., Li, Y., Drake, T. W., ... others (2026). Large underestimation of smallholder agriculture in the tropics by classic remote sensing products: Evidenced from the kasaï river basin. *Environmental Research Communications*.

Supplementary Information for "Silicate Weathering Dynamics in the Kasaï Basin and Implications for Enhanced Rock Weathering Applications in the Tropics"

Yi Hou[1*], Lissie de Groot[2], Travis Drake[2], José Nlandu Wabakanghanzi[3], Alfred Ludjwera Bahati[4], Marijn Bauters[5], Chris Seitz[6], Antoine de Clippele[2], Johan Six[2], Kristof Van Oost[7], Jordon D. Hemingway[1]

[1]Geological Institute, Department of Earth and Planetary Sciences, ETH Zurich, Zurich, Switzerland; [2]Institute of Agricultural Sciences, Department of Environmental Systems Science, ETH Zurich, Zurich, Switzerland; [3]Department of Soil Physics and Hydrology, Congo Atomic Energy Commission, Kinshasa, Democratic Republic of Congo; [4]Régie des Voies Fluviales, Kinshasa, Democratic Republic of Congo; [5]Q-ForestLab, Department of Environment, Ghent University, Ghent, Belgium; [6]Institute of Geochemistry and Petrology, Department of Earth and Planetary Sciences, ETH Zurich, Zurich, Switzerland; [7]Earth and Life Institute, Université catholique de Louvain, Louvain-la-Neuve, Belgium

[*]To whom correspondence and requests for materials should be addressed: yihouy@ethz.ch

Contents of this file

Table S2 Details on sample processing, storage, and handling of the different aliquots

1 Sample collection and field observations

1.1 Sample collection

River water samples were collected either with a Van Dorn sampler or 1 L high density polyethylene (HDPE) bottles (only in the dry season of 2024). Samples were filtered with Teflon-coated pressure filtration towers and Nalgene vacuum filtration units with 0.2 μm nylon or polyethersulfone (PES) or nitrocellulose mixed ester (MCE) membrane filters into different aliquots for different chemical and isotopic analyses of the dissolved load. Full details on the processing and storage of the different sample aliquots can be found in Supplementary Table 2. Weighed river water was filtered with a Nalgene vacuum filtration unit through combusted (450 °C, 5 hours), pre-weighed 0.7 μm glass fiber filters (*Whatman GF/F*). Approximately 1 L of river water was passed through each filter and three filters were collected for each sample.

For dissolved inorganic carbon (DIC) concentration and stable carbon isotope ($\delta^{13}C$) measurements, 6 mL of water was collected directly from the Van Dorn sampler into a syringe with no headspace and immediately filtered through a syringe filter (0.22 μm PTFE/L, *Avantor*, USA). The filtrate was injected into 12 mL exetainers (*Labco*, UK), which had been poisoned with 50 μL 50% $ZnCl_2$, acidified with 50 μL H_3PO_4, and flushed with N_2. Triplicate exetainer vials were collected for each sample.

Water temperature, pH, dissolved oxygen (DO), fluorescent dissolved organic matter (fDOM), and turbidity were measured with a multiprobe (*EXO2 YSI, Xylem*, USA) and can be found in the dataset published along this manuscript on `Zenodo`.

1.2 Discharge and suspended sediment concentration

Discharge was measured using a *SonTek RiverSurveyor Rs5* or *M9* Acoustic Doppler Current Profiler (ADCP) mounted to a motorized wooden canoe. Reported discharge values represent the average of four transects, the coefficient of variation of which never exceeded 1.3%.

Total suspended sediment (TSS) concentration was calculated with the weight of sediments collected onto the GFF filters and the volume of filtered river water. Sediment flux and erosion rate (sediment flux normalized to catchment area assuming an upper continental crust density of 2.8 g cm^{-3}) were then calculated with measured discharge and TSS concentration.

2 Chemical and isotopic analyses

2.1 Major cation, anion, dissolved Si and dissolved organic carbon (DOC)

The concentrations of major cations (Na^+, Mg^{2+}, K^+, Ca^{2+}) were measured with an Inductively Coupled Plasma-Mass Spectrometer (ICP-MS, *Thermo Scientific Element 2*). To avoid matrix effects from high DOC content, 10 mL of water samples were dried in teflon vials and subsequently fluxed with concentrated trace metal grade nitric acid and hydrogen peroxide for two or three cycles. Samples were then re-dissolved in nitric acid. Indium was added as an internal standard prior to analyses. Measurements of two reference materials (SLRS, *Canadian Research Council* and SGR-1, *United States Geological Survey*) matched certified and previously reported values within analytical uncertainties (Gladney & Roelandts, 1988). Precision is estimated to be better than 10% for Na^+, Mg^{2+}, K^+, and 11% for Ca^{2+} ($\pm 2\sigma$) based on duplicate measurements of a subset of 10 samples within and between analytical sessions.

Dissolved Si (as silicic acid, $Si(OH)_4$) concentrations were measured colorimetrically using a UV-Vis spectrophotometer (*Unicam*; Mullin & Riley, 1955). Measurements of two reference materials (SLRS-6 and PERADE-07, *Canadian Research Council*) matched previously certified and previously reported values

(Yeghicheyan et al., 2019). Precision is estimated to be less than 4% ($\pm 2\sigma$) based on dupliate measurements of eight samples.

Major anion (Cl^-, SO_4^{2-}, NO_3^-) concentrations were measured by ion chromatography (*Thermo Scientific Dionex Aquion* with an *AG9-HC* guard column and an *AS9-HC* analytical column). Precision was estimated to be better than 5% for Cl^- and 10% for SO_4^{2-} ($\pm 2\sigma$) from triplicate measurements of two samples. Measurements of a reference material (BIGMOOSE-14, *Canadian Research Council*) agree with certified values within analytical uncertainties.

DOC concentrations were determined via high-temperature catalytic oxidation using a total organic carbon analyzer (*Shimadzu TOC-L*) fitted with a *TNM-1* module following methods described in (Drake et al., 2018).

2.2 Alkalinity

Total alkalinity (TA) was measured by Gran titration (Gran, 1952) using a manual digital titrator (*Hach*) with 0.16 N sulfuric acid (H_2SO_4) on an aliquot of ~100 mL filtrate water (0.2 μm PES or nylon filters), usually within one week of sample collection. Two calcium carbonate standards (0.1 mEq L^{-1} and 1 mEq L^{-1}) (n = 5 each) were measured as 0.095 $\pm$ 0.011 mEq L^{-1} amd 0.948 $\pm$ 0.075 mEq L^{-1}, respectively ($\pm 2\sigma$). The higher relative standard deviation (11.8%) was assigned as the uncertainties of the alkalinity measurements by titration. TA was also independently calculated with charge balance as

$$\begin{aligned} \mathrm{TA} &= \sum \text{conservative cations} - \sum \text{conservative anions} \\ &= [\mathrm{Na^+}] + [\mathrm{K^+}] + 2 \times [\mathrm{Mg^{2+}}] + 2 \times [\mathrm{Ca^{2+}}] - [\mathrm{Cl^-}] - 2 \times [\mathrm{SO_4^{2-}}] - [\mathrm{NO_3^-}], \end{aligned} \tag{1}$$

where square brackets indicate molar concentrations.

Alkalinity measured by Gran titration and calculated by charge balance match well except for samples with low pH and high DOC as well as samples collected in the dry season of 2024 (Figure S8). Discrepancies between alkalinity estimated by the two methods for the low pH samples enriched in DOC likely stem from the well-documented increasing inaccuracy of the Gran titration method at lower pH (Neal, 2001; Wang et al., 2013). For samples collected in the dry season of 2024, the disagreement instead likely results from filter size inconsistencies: an operational error led to alkalinity being measured with aliquots of 0.7 μm filtrate water, whereas the dissolved major cations and anions of all samples were measured with aliquots of 0.2 μm filtrate water. We therefore opted to use alkalinity estimated by charge balance in all subsequent calculations to ensure internal consistency.

Carbonate alkalinity ($[HCO_3^-]$ + $2\times[CO_3^{2-}]$) was calculated from CO2SYS (Lewis & Wallace, 1998; Van Heuven, Pierrot, Rae, Lewis, & Wallace, 2011; Sharp et al., 2020) using the freshwater option with measured water temperature, pH, and DIC concentration of each sample. The water temperature measurement of sample R24 in the dry season was missing from our field notes; for the carbonate speciation calculations of this sample, we assumed it to be the same as the water temperature of sample R23 collected nearby (i.e., $<$ 2 km between sample sits) and on the same day.

2.3 Stable oxygen and deuterium isotopic composition of water

Stable oxygen and deuterium isotopic compositions ($\delta^{18}O$ and δ^2H) of water were measured using a high-temperature conversion periphery (*Finnigan* TC/EA) coupled to a *Finnigan DELTAplus XP* isotope ratio mass spectrometer (IRMS) via a *Finnigan ConFlo III* interface following previously published method (Gehre, Geilmann, Richter, Werner, & Brand, 2004). Briefly, 0.5 μL water is injected into the TC/EA via a *CTC PAL* autosampler equipped with a 10 μL gas-tight syringe (pre-washed 3$\times$) where it is converted to H_2 and CO gases and chromatographically separated; δ^2H and $\delta^{18}O$ were thus measured using a single

injection via "peak jumping", and samples were analyzed in triplicate. In-house standards were analyzed in each sequence identically to unknown samples and are calibrated to Vienna Standard Mean Ocean Water (VSMOW) and Standard Light Antarctic Precipitation (SLAP) values of 0 ‰ and -428 ‰ for δ^2H and 0 ‰ and -55.5 ‰ for δ^{18}O, respectively (Coplen, 1988), using international water reference materials provided by the International Atomic Energy Agency (IAEA, Austria). Post-analysis offline calculation and offset, memory, and drift correction were achieved following the "identical treatment principle" of (Werner & Brand, 2001). Long-term precision of in-house standards is ±0.6 ‰ for δ^2H and ±0.2 ‰ for δ^{18}O across all sequences ($\pm 1\sigma$).

3 Inverse mass balance modeling of river solutes

The software *MEANDIR* (Kemeny & Torres, 2021) was used for the mass balance modeling of river solutes in this work. As the code packages are freely accessible (see the "Code Availability and Data Sources" section in Kemeny & Torres, 2021), details below mainly focus on parameter choice and model implementation.

End-member compositions used in the model can be found in Supplementary Table 2. Uniform distributions between assigned minimum and maximum values were used as prior distributions for all end members. Solutes were normalized to the sum of major cation (Na^+, K^+, Ca^{2+}, Mg^{2+}) concentrations, as well as sulfate (SO_4^{2-}) concentration, as we explicitly track pyrite weathering contributions. We performed a sufficient number of simulations to generate 200 successful results for each river sample, where a successful result is a model simulation that matched all solute observations within 15%. In a set of preliminary tests, we generated 1000 model results for a subset of samples and verified that 200 results were sufficient for characterizing the posterior distributions.

While the end-member compositions of precipitation, silicate, carbonate, and pyrite weathering are readily available from the literature (Berner & Berner, 2012; Gaillardet, Dupré, Louvat, & Allegre, 1999; Burke et al., 2018; Kemeny & Torres, 2021), the composition of throughfall is less constrained and exhibits more spatial variability (Bauters et al., 2021; De Schrijver et al., 2007). The throughfall end-member composition used in this work was obtained from a time-series of 2-year field measurements in the Yoko Forest Reserve (0°17'N, 25°18'E) in the Congo Basin (Makelele et al., 2022; Bauters et al., 2022), where the 10^{th} – 90^{th} percentile of the elemental ratios were assigned as the minimum and maximum values of the prior distribution. We acknowledge that the throughfall data were collected from outside of the Kasaï Basin, but we consider these compositions to be representative since the central Congo Basin – which contains the Yoko Forest Reserve – shares broadly similar climatic, hydrologic, and geologic conditions with the Kasaï Basin.

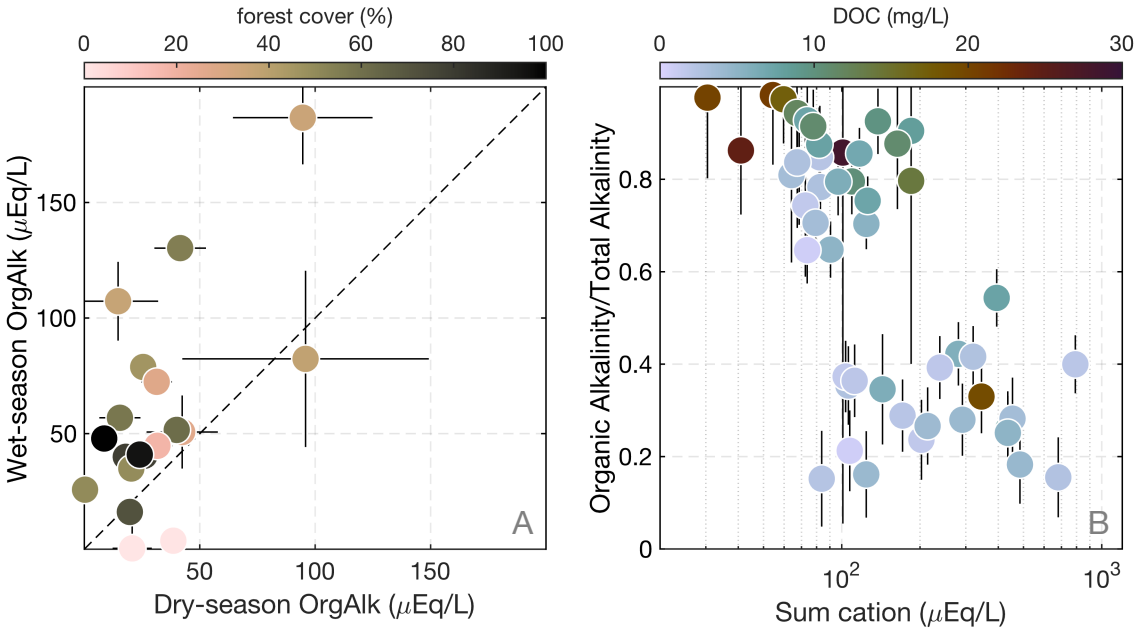

Supplementary Figure 1: (A) Comparison between wet and dry season organic alkalinity (OrgAlk), color coded by percentage of forest cover. (B) The fraction of OrgAlk as a function of total cation load, color coded by DOC concentration.

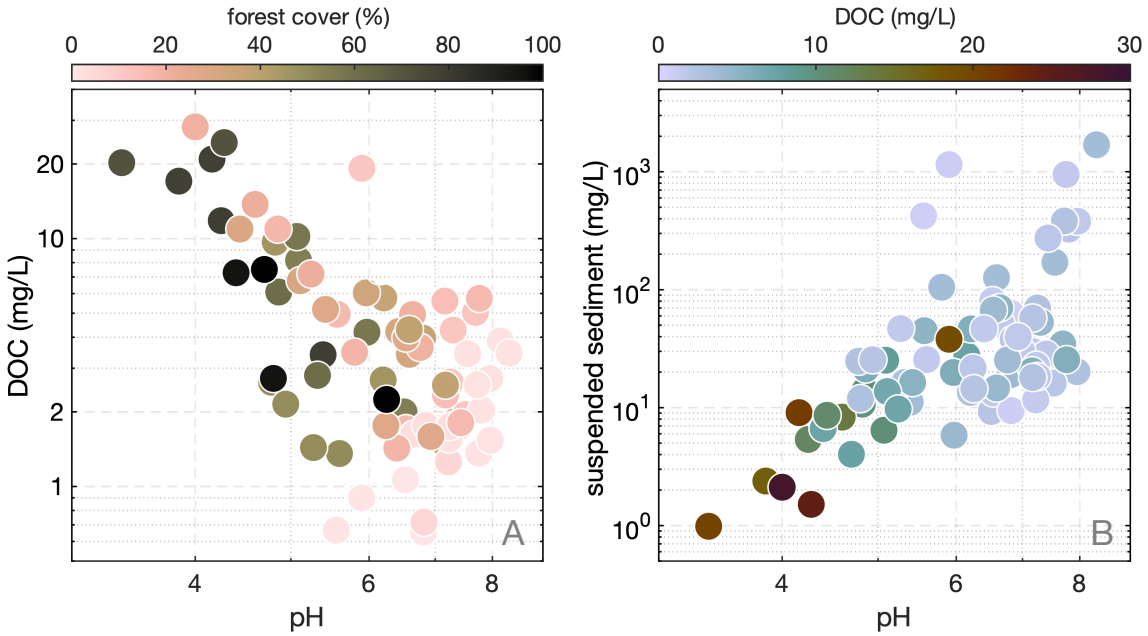

Supplementary Figure 2: Cross plots of (A) DOC concentration vs. pH, color coded by percentage of catchment forest cover; (B) Suspended sediment concentration vs. pH, color coded by DOC concentration.

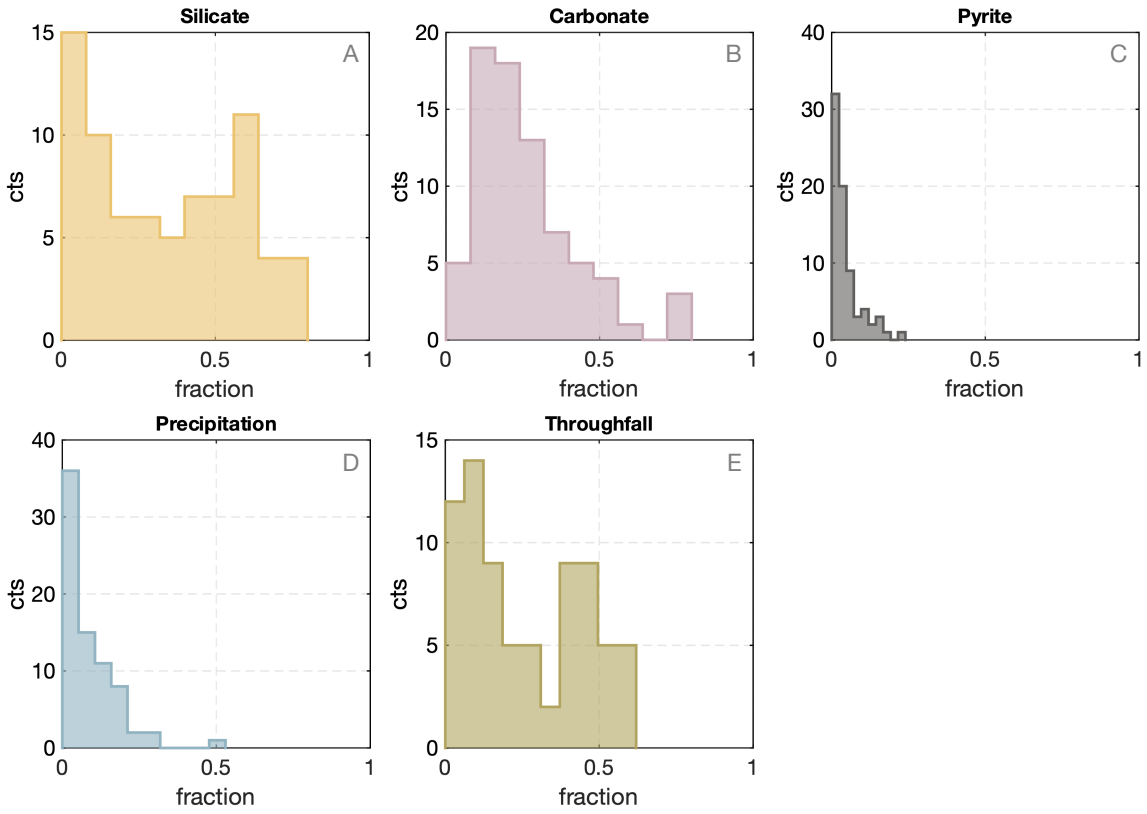

Supplementary Figure 3: Estimated fractional contribution of (A) silicate weathering, (B) carbonate weathering, (C) pyrite weathering, (D) precipitation, and (E) throughfall end members to river solutes (major cations + sulfate) from mass balance modeling of all river samples.

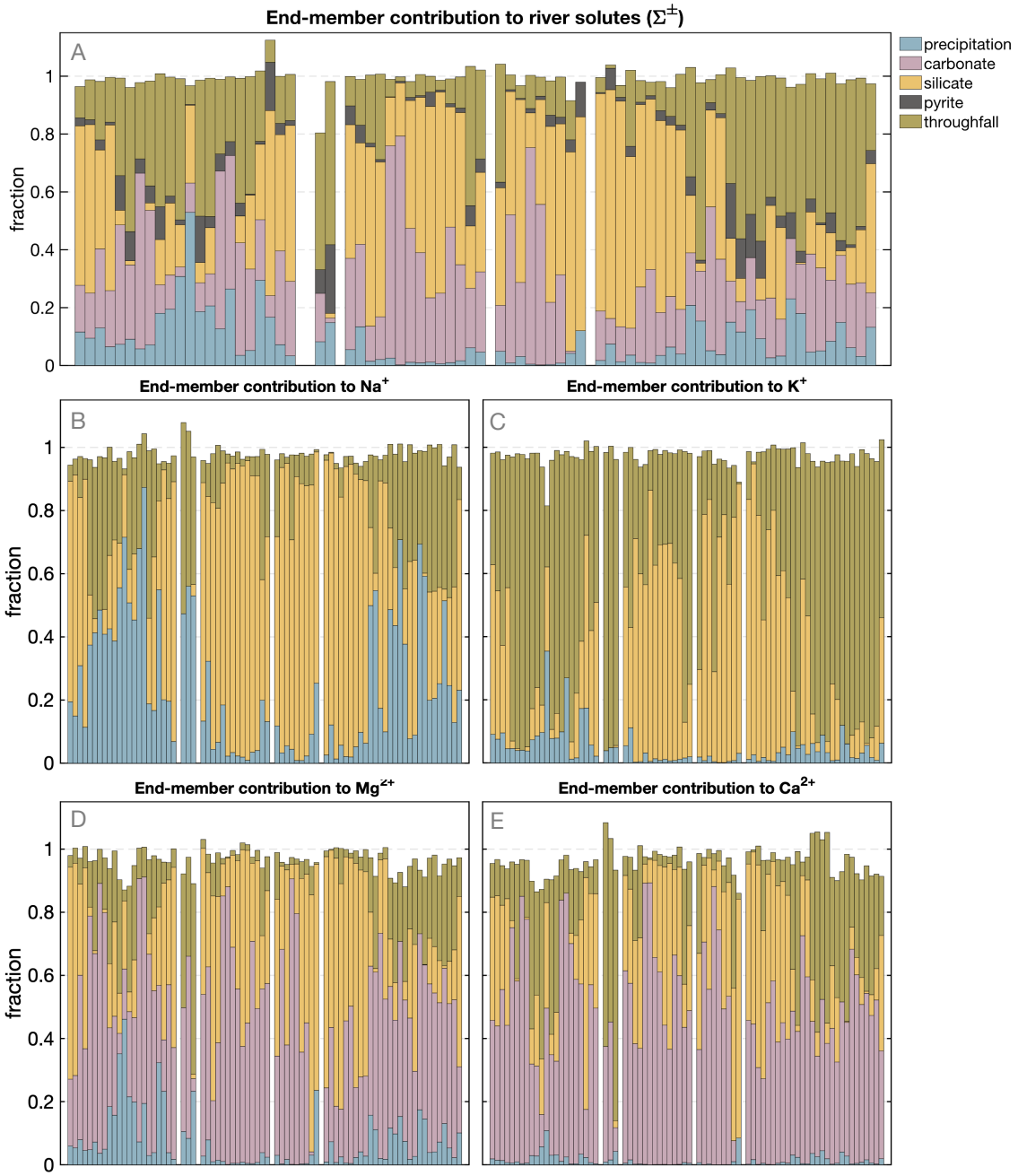

Supplementary Figure 4: Results of mass-balance modeling of river solutes. Estimated end-member contributions to (A) cations + sulfate, (B) Na^{+}, (C) K^{+}, (D) Mg^{2+}, and (E) Ca^{2+}, calculated as the median of all successful simulations for each sample ($n = 200$).

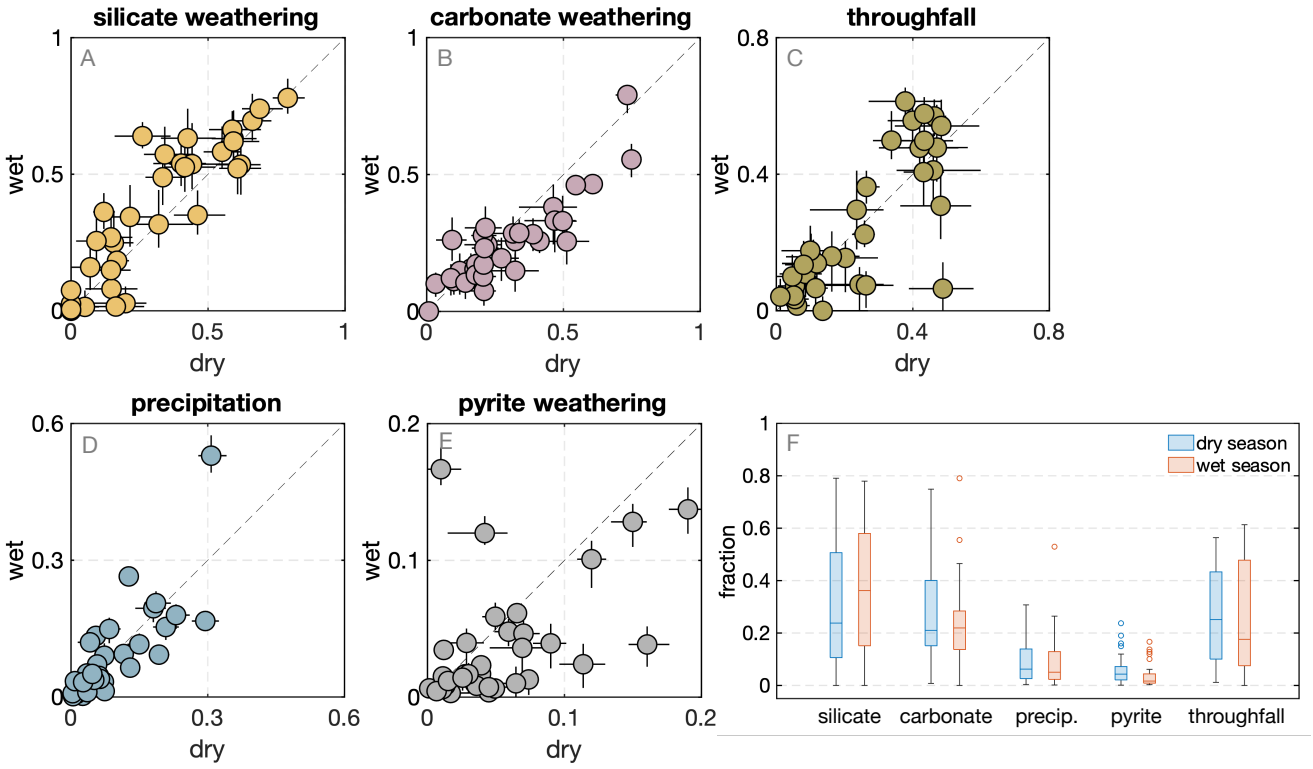

Supplementary Figure 5: Comparison of fractional contribution from (A) silicate weathering, (B) carbonate weathering, (C) precipitation, (D) pyrite weathering, and (E) throughfall between dry and wet season. Error bars represent 25th – 75th percentile of successful simulations. Dashed lines are 1:1 lines. (F) Box plot summarizing the dry vs. wet season comparison by different end members.

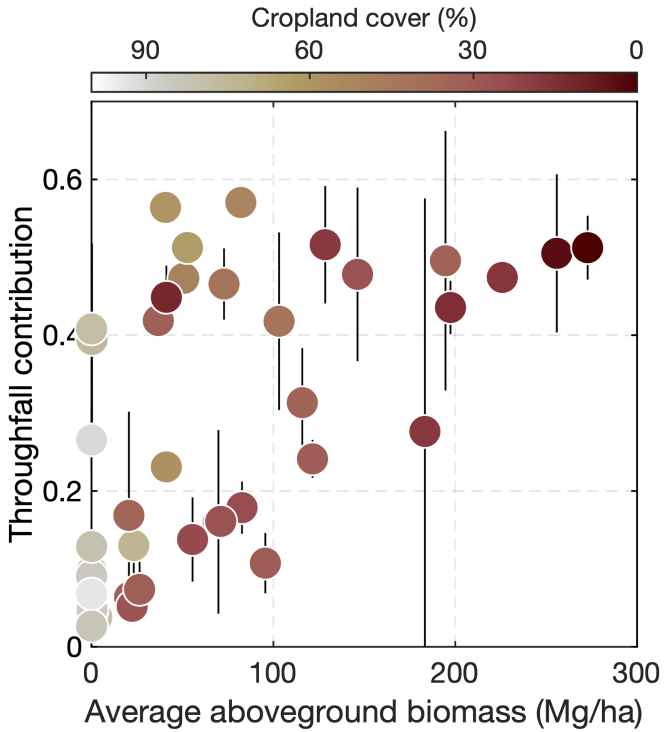

Supplementary Figure 6: Correlation (Spearman's $\rho = 0.63$, $p = 1.1 \times 10^{-5}$) between estimated fractional contribution from throughfall and catchment-averaged aboveground biomass (Mg ha^{-1}). Data products from European Space Agency (ESA) Climate Change Initiative (CCI) Biomass project (Santoro & Cartus, 2025) were used to estimate the aboveground biomass in the Kasai Basin.

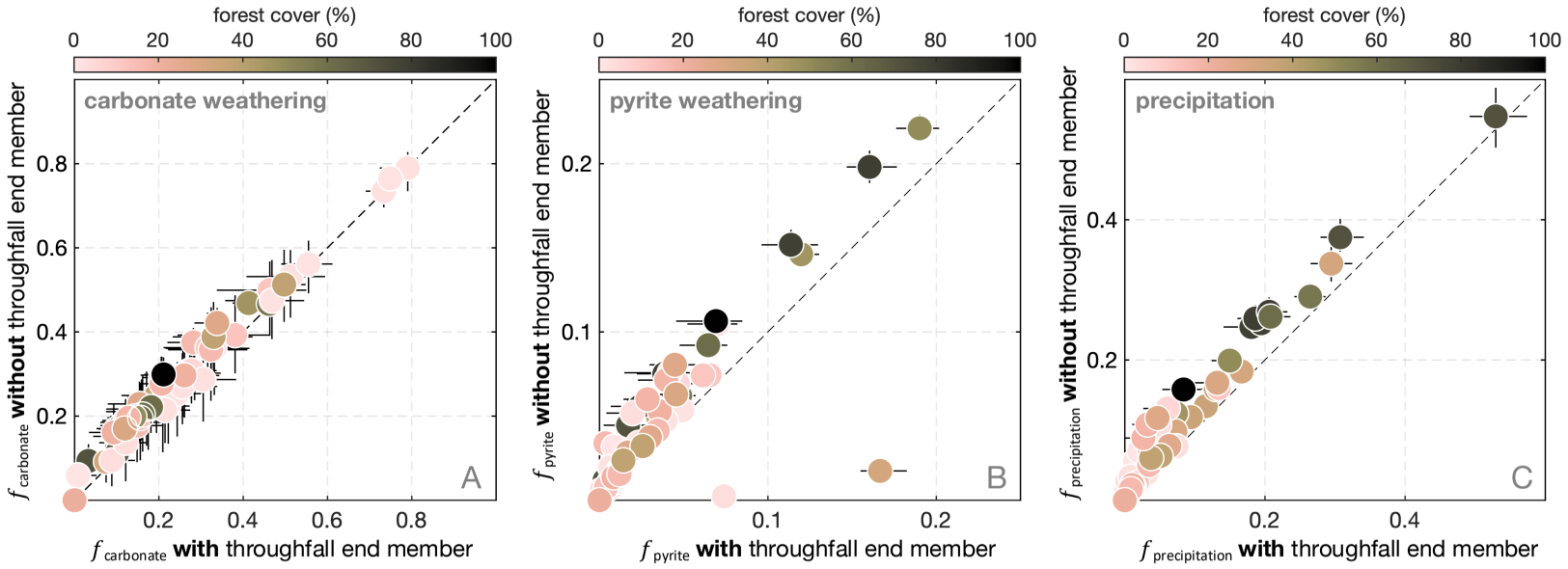

Supplementary Figure 7: Estimated fractional contribution of (A) carbonate weathering, (B) pyrite weathering, and (C) precipitation from inverse modeling where throughfall is included or excluded as an end member, color coded by percentage of catchment forest cover. Error bars represent 25th – 75th percentile of all successful simulations. Dashed lines are 1:1 lines.

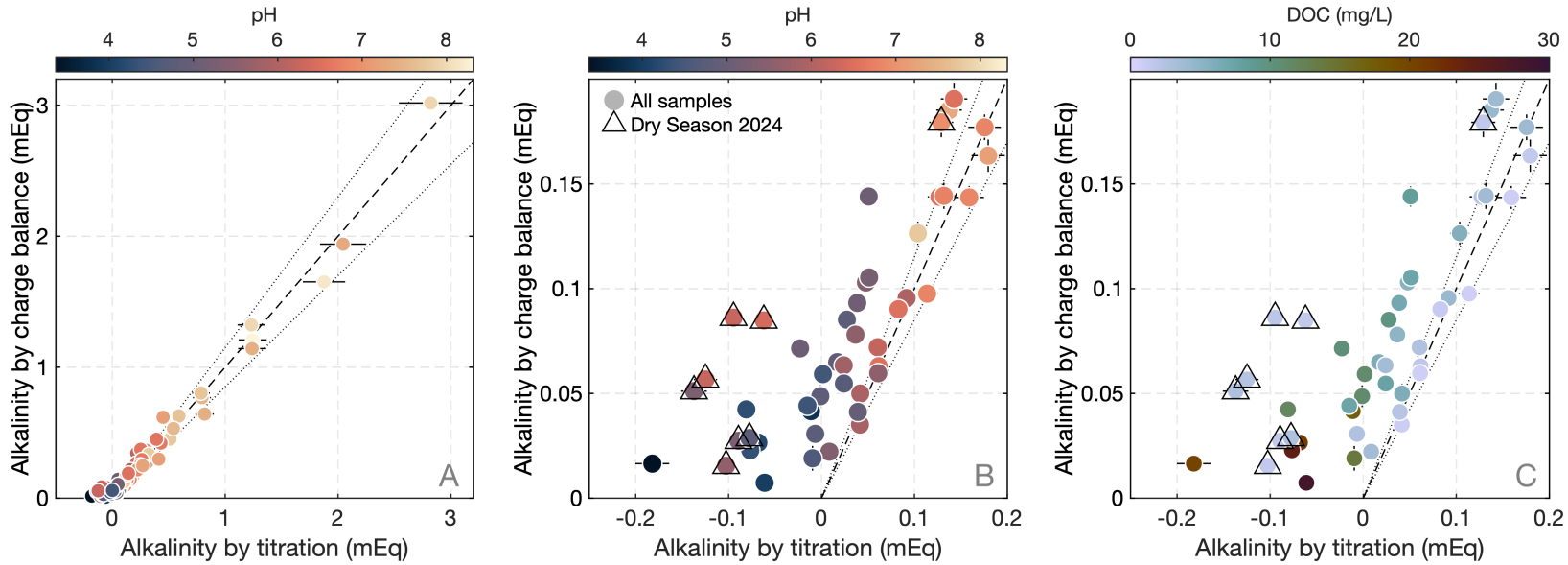

Supplementary Figure 8: Comparison between alkalinity measured by Gran titration and calculated by charge balance of (A) all samples, and samples with low alkalinity, color coded by (B) pH and (C) DOC concentration. In all panels, dashed lines are 1:1 lines with dotted lines representing 15% deviations. The two independent methods yield similar results except for samples with low pH/high DOC content and samples collected in the dry season of 2024. The discrepancies between alkalinity estimated by two methods for the low pH samples enriched in DOC likely stem from increasing inaccuracy of the Gran titration at lower pH (Neal, 2001; Wang et al., 2013). For the samples collected in the dry season of 2024, the disagreement likely resulted from filtration inconsistencies – while the dissolved major cations and anions were measured with aliquots of samples passed through 0.2 μm filters, alkalinity was measured with aliquots of 0.7 μm filtrates.

Supplementary Table 1: End member compositions used in the solute mass balance model.

		Silicate	**Carbonate**	**Pyrite**	**Precipitation**	**Throughfall**
$Na^+/\sum^{\pm}$	min	0.209	0	0	0.6	0.069
$Na^+/\sum^{\pm}$	max	0.677	0	0	0.9	0.33
$K^+/\sum^{\pm}$	min	0.02	0	0	0.01	0.23
$K^+/\sum^{\pm}$	max	0.6	0	0	0.2	0.611
$Ca^{2+}/\sum^{\pm}$	min	0.039	0.325	0	0.01	0.123
$Ca^{2+}/\sum^{\pm}$	max	0.591	1	0	0.06	0.299
$Mg^{2+}/\sum^{\pm}$	min	0	0	0	0.07	0.055
$Mg^{2+}/\sum^{\pm}$	max	0.466	0.675	0	0.2	0.12
$Cl^-/\sum^{\pm}$	min	0	0	0	0.8	0.079
$Cl^-/\sum^{\pm}$	max	0	0	0	1.1	0.254
$SO_4^{2-}/\sum^{\pm}$	min	0	0	1	0.015	0.050
$SO_4^{2-}/\sum^{\pm}$	max	0	0	1	0.15	0.150

Supplementary Table 2: Details on sample processing, storage, and handling of the different aliquots.

Aliquot/Analyses	**Container**	**Volume (mL)**	**Storage**	**Acidified to pH 2 w/ conc. HCl**
Cations	high density polyethylene (HDPE) bottle	60	refrigerated	in the field or before analyses
Anions	HDPE bottle	60	refrigerated	N/A
Nutrients	HDPE bottle	125	frozen	N/A
Dissolved organic carbon (DOC)	HDPE bottle	250	refrigerated	in the field
Trace metals and their isotopes	acid washed HDPE bottle	500/1000	room temperature	back at ETH*
Water isotopes	exetainer	3	refrigerated	N/A
Dissolved inorganic carbon (DIC)	exetainer	6	refrigerated	N/A
Alkalinity	HDPE bottle	100	N/A	N/A

All aliquots filtered through 0.2 μm filters.
*: usually within one month of sample collection

References

Bauters, M., Drake, T. W., Wagner, S., Baumgartner, S., Makelele, I. A., Bodé, S., ... Boeckx, P. (2021). Fire-derived phosphorus fertilization of african tropical forests. *Nature Communications*, *12*(1), 5129.

Bauters, M., Janssens, I. A., Wasner, D., Doetterl, S., Vermeir, P., Griepentrog, M., ... Boeckx, P. (2022). Increasing calcium scarcity along afrotropical forest succession. *Nature Ecology & Evolution*, *6*(8), 1122–1131.

Berner, E. K., & Berner, R. A. (2012). *Global environment: water, air, and geochemical cycles*. Princeton University Press.

Burke, A., Present, T. M., Paris, G., Rae, E. C., Sandilands, B. H., Gaillardet, J., ... Adkins, J. F. (2018). Sulfur isotopes in rivers: Insights into global weathering budgets, pyrite oxidation, and the modern sulfur cycle. *Earth and Planetary Science Letters*, *496*, 168–177.

Coplen, T. B. (1988). Normalization of oxygen and hydrogen isotope data. *Chemical Geology: Isotope Geoscience Section*, *72*(4), 293–297.

De Schrijver, A., Geudens, G., Augusto, L., Staelens, J., Mertens, J., Wuyts, K., ... Verheyen, K. (2007). The effect of forest type on throughfall deposition and seepage flux: a review. *Oecologia*, *153*(3), 663–674.

Drake, T. W., Guillemette, F., Hemingway, J. D., Chanton, J. P., Podgorski, D. C., Zimov, N. S., & Spencer, R. G. (2018). The ephemeral signature of permafrost carbon in an Arctic fluvial network. *Journal of Geophysical Research: Biogeosciences*, *123*, 1475–1485.

Gaillardet, J., Dupré, B., Louvat, P., & Allegre, C. (1999). Global silicate weathering and CO_2 consumption rates deduced from the chemistry of large rivers. *Chemical geology*, *159*(1-4), 3–30.

Gehre, M., Geilmann, H., Richter, J., Werner, R., & Brand, W. (2004). Continuous flow $^{2}H/^{1}H$ and $^{18}O/^{16}O$ analysis of water samples with dual inlet precision. *Rapid communications in mass spectrometry*, *18*(22), 2650–2660.

Gladney, E. S., & Roelandts, I. (1988). 1987 compilation of elemental concentration data for USGS BHVO-1, MAG-1, QLO-1, RGM-1, SCo-1, SDC-1, SGR-1 and STM-1. *Geostandards Newsletter*, *12*(2), 253–362.

Gran, G. (1952). Determination of the equivalence point in potentiometric titrations. Part II. *Analyst*, *77*(920), 661–671.

Kemeny, P. C., & Torres, M. A. (2021). Presentation and applications of mixing elements and dissolved isotopes in rivers (MEANDIR), a customizable MATLAB model for Monte Carlo inversion of dissolved river chemistry. *American Journal of Science*, *321*(5), 579–642.

Lewis, E., & Wallace, D. (1998). *Program developed for CO_2 system calculations* (Tech. Rep.). Environmental System Science Data Infrastructure for a Virtual Ecosystem.

Makelele, I. A., Bauters, M., Verheyen, K., Barthel, M., Six, J., Rütting, T., ... Boeckx, P. (2022). Conservative N cycling despite high atmospheric deposition in early successional african tropical lowland forests. *Plant and Soil*, *477*(1), 743–758.

Mullin, J., & Riley, J. (1955). The colorimetric determination of silicate with special reference to sea and natural waters. *Analytica Chimica Acta*, *12*, 162–176.

Neal, C. O. (2001). Alkalinity measurements within natural waters: towards a standardised approach. *Science of the Total Environment*, *265*(1-3), 99–113.

Santoro, M., & Cartus, O. (2025). *ESA Biomass Climate Change initiative (Biomass_cci): Global datasets of forest above-ground biomass for the years 2007, 2010, 2015, 2016, 2017, 2018, 2019, 2020, 2021 and 2022, v6.0.* NERC EDS Centre for Environmental Data Analysis. Retrieved from https://catalogue.ceda.ac.uk/uuid/95913ffb6467447ca72c4e9d8cf30501

Sharp, J., Pierrot, D., Humphreys, M., Epitalon, J., Orr, J., Lewis, E., & Wallace, D. (2020). *CO_2-SystemExtd, v3. 0.1, MATLAB (MathWorks).*

Van Heuven, S., Pierrot, D., Rae, J., Lewis, E., & Wallace, D. (2011). MATLAB program developed for CO_2 system calculations. *(No Title)*.

Wang, Z. A., Bienvenu, D. J., Mann, P. J., Hoering, K. A., Poulsen, J. R., Spencer, R. G., & Holmes, R. M. (2013). Inorganic carbon speciation and fluxes in the Congo River. *Geophysical Research Letters*, *40*(3), 511–516.

Werner, R. A., & Brand, W. A. (2001). Referencing strategies and techniques in stable isotope ratio analysis. *Rapid Communications in Mass Spectrometry*, *15*(7), 501–519.

Yeghicheyan, D., Aubert, D., Bouhnik-Le Coz, M., Chmeleff, J., Delpoux, S., Djouraev, I., ... Suchorski, K. (2019). A new interlaboratory characterisation of silicon, rare earth elements and twenty-two other trace element concentrations in the natural river water certified reference material SLRS-6 (NRC-CNRC). *Geostandards and Geoanalytical Research*, *43*(3), 475–496.